Rain Nowcasting from Multiscale Radar Images

Aniss Zebiri[1], Dominique Béréziat[1], Etienne Huot[2] and Isabelle Herlin[3]

[1]*Sorbonne Université, CNRS, Laboratoire d'Informatique de Paris 6, France*

[2]*Université de Versailles Saint-Quentin-en-Yvelines, LATMOS/IPSL, France*

[3]*Inria, France*

Keywords: Rain Forecasting, Weather Radar, Multiscale Image, Image Assimilation, Motion Estimation.

Abstract: Rainfall forecasting is a major issue for anticipating severe meteorological events and for agriculture management. Weather radar imaging has been identified in the literature as the best way to measure rainfall on a large domain, with a fine spatial and temporal resolution. This paper describes two methods allowing to improve rain nowcast from radar images at two different scales. These methods are further compared to an operational chain relying on only one type of radar observation. The comparison is led with regional and local criteria. For both, significant improvements are quantified compared to the original method.

1 INTRODUCTION

In meteorology, precipitation forecast is a major issue. In case of short term forecast, with a time horizon lower than 2 hours, it is usually called nowcast. Rainfall nowcast is known to be of major interest for severe events anticipation (Joe et al., 2012) and for agriculture (Stigter et al., 2000).

Different rainfall forecasting methods are available, ranging from sophisticated numerical weather prediction (NWP) models to simple extrapolation of images acquired by satellites or radars. The constraints of temporal horizon and spatial scale of the weather structure dictate the type of methods that can be successfully applied. NWP models are daily computing weather forecasts: starting from initial conditions that are derived, the future state of the atmosphere is estimated from the integration in time of evolution equations. Nowadays, most of NWP models involve data assimilation methods for improving results from observations (Le Dimet and Talagrand, 1986; Courtier et al., 1994). The computing time required by NWPs is usually large and a few hours is required since the last observations acquisition for providing a forecast. Assimilating high-resolution data with a high-resolution NWP model in a short-cycle mode is a challenging issue that has not yet been reached. On another hand, extrapolation methods based on image acquisitions quickly provide an efficient result if the forecast horizon is short enough. Two types of image extrapolation approaches can be used, depending on their motion estimation component, which is based either on structure tracking or on dense motion estimation. The tracking approach (Dixon and Wiener, 1993; Johnson et al., 1998) first identifies rain structures as characteristic features of the image and evaluates their displacement by identifying the same features in successive images, often with a cross-correlation technique. The dense approach is based on the optical flow technique (Horn and Schunk, 1981; Béréziat et al., 2000; Germann and Zawadzki, 2002; Bowler et al., 2004; Héas et al., 2007; Berenguer et al., 2011). However, most motion estimation processes do not include a physical model on the rain evolution and the quality of their results remain low. During the last decade, an alternative approach of motion estimation came from the data assimilation technique. In the context of rain nowcast, this *image assimilation* approach (Le Dimet et al., 2006; Korotaev et al., 2008; Corpetti et al., 2009; Titaud et al., 2010; Huot et al., 2013) offers the possibility to compute an optimal solution from all types of information: outputs of an NWP model, satellite images, radar images, rain gauges measures. Moreover, motion estimation with *image assimilation* allows to combine the dense and feature-based approaches and relies simultaneously on raw observational images and characteristic features, resulting in a better estimation (Lepoittevin et al., 2013).

In this paper, we describe two methods of multiscale rain nowcasting, relying on image assimilation of images with different spatial resolution. The two

methods derive from an initial work of (Lepoittevin and Herlin, 2015) that is operationally used by the French StartUp Weather Measures [1] and referenced as the RainNowcast (RN) chain in the following. In this approach, motion is first estimated on a short temporal window of image acquisitions; then, the last available image is transported by the velocity map providing a synthetic image at a chosen time horizon. The first multiscale method is a serial one: motion estimation is first estimated from regional images, at small resolution, and then refined with local images, at large resolution. The second method allows to assimilate simultaneously local and regional images at both resolutions.

The paper is organized as follow: Section 2 described data and their major characteristics. Section 3 summaries the initial RN method, while Section 4 describes our methodological contributions for combine local and regional data. Section 5 displays results and evaluates the performance of the multiscale methods both compared to RN results and to the ground truth. Concluding remarks and future research directions are given in Section 6.

2 DATA

The radar reflectivity is directly linked to the rain rate (Marshall and Palmer, 1948). Most of the meteorological radar networks, as the French PANTHERE network operated by Météo France include sensors, providing long distance measures. These radars, usually working in C or S-BAND frequency ranges, allow a large regional coverage. However, their low spatial resolution (1 km) is a major drawback for local applications. X-BAND sensors, as operated by Weather Measures, are smaller and provide more accurate measures but at a shorter range.

The objective is to combine the PANTHERE regional images with the X-BAND local images for an improved rain forecast. Both types of images are acquired each 5 minutes and projected on the same Cartesian grid at the X-BAND resolution (200 m). Figure 1 compares PANTHERE to X-BAND images (the legend gives the color code used to express the rain rate in mm/h): X-BAND images are more precise but the PANTHERE domain is larger.

In this paper, we focus on a severe rainfall event that occurred in June 2016. The set of images has been acquired between 24th at 4 pm and 25th at 3 am. The size of the PANTHER data is 196×234 pixels cropped from the original image and centered over the
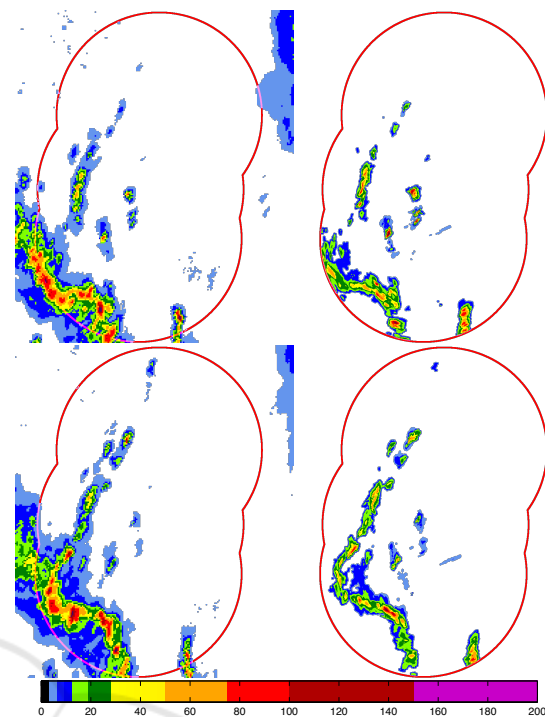
---

[1] https://www.weather-measures.fr/

Figure 1: Rainfall event at two spatial resolutions. Left: PANTHERE data, right: X-BAND data. The red contour corresponds to the limit of the X-BAND domain. Top: acquisition at 4 pm. Bottom: at 4:15 pm.

local domain that has a size of 980×1170 pixels. The local domain covers 64% of the regional domain.

3 RAIN NOWCAST (RN)

This reference method is based on two main steps.

In a first one, a velocity field is estimated from four consecutive reflectivity radar images. The method is based on data assimilation and take into account a model of the dynamics observed by the images. It has been proved to be competitive compared to the classic optical flow based approaches (Béréziat, 2018). Once the velocity map computed, the next step transports the last image observation, according to the advection equation, up to the chosen temporal horizon. At each new acquisition, the velocity is updated and a new forecast is delivered, thanks to a sliding window technique. The Weather Measures company runs this process operationally.

In the following subsections, we briefly summarize the method, see (Lepoittevin and Herlin, 2015) for additional details.

3.1 Motion Estimation (ME)

Let define $\mathbf{X} = \begin{pmatrix} \mathbf{w}^T & I \end{pmatrix}$ the state vector. $\mathbf{w} = \begin{pmatrix} u & v \end{pmatrix}^T$ is the velocity map, I is a synthetic image having the same properties than image acquisitions and T is the transpose operator. $(\mathbf{x},t) \mapsto \mathbf{X}(\mathbf{x},t)$ is an integrable function defined over Ω, the image domain, and on $[t_0, t_3]$, the temporal interval of image acquisition. Observations are reflectivity images. They are sparse in time. Four observations, denoted $O(t_i)$ with $i = 0, 1, 2, 3$, are used for estimating velocity. Motion estimation is modeled as the solution of the following system of equations:

$$\frac{\partial \mathbf{X}}{\partial t}(\mathbf{x},t) + \mathbb{M}(\mathbf{X})(\mathbf{x},t) = 0, \ (\mathbf{x},t) \in \Omega \times]t_0, t_3] \quad (1)$$

$$\mathbf{X}(\mathbf{x},t_0) - \mathbf{X}_b(\mathbf{x}) = \varepsilon_B(\mathbf{x}) \quad (2)$$

$$\mathbb{H}(\mathbf{X})(\mathbf{x},t) - O(\mathbf{x},t) = \varepsilon_R(\mathbf{x},t), \text{ if } t = t_i. \quad (3)$$

The first equation, Eq. (1), describes the temporal dynamics of the state vector and the knowledge available on studied the system, either physical laws or heuristics hypothesis. Here, we assume:

1. the synthetic image I is transported by the velocity map $\mathbf{w}$. This is modeled by the advection equation: $\frac{\partial I}{\partial t}(\mathbf{x},t) + \nabla I(\mathbf{x},t).\mathbf{w}(\mathbf{x},t) = 0$ with ∇ the gradient operator,

2. the velocity is stationary on a short time interval, so: $\frac{\partial \mathbf{w}}{\partial t}(\mathbf{x},t) = \vec{0}$;

With such hypothesis, $\mathbb{M}$ is defined by $\mathbb{M}(\mathbf{X}) = \begin{pmatrix} \vec{0} & \nabla I.\mathbf{w} \end{pmatrix}^T$.

The second equation, Eq. (2), describes the knowledge given on the initial condition of the state vector, $\mathbf{X}(t_0)$. $\mathbf{X}_b$ is called *background*. I_b is taken as the first available image observation, $I_b(t_0) = O(t_0)$, and $\mathbf{w}_b$ is either $\vec{0}$ or the value estimated on the previous window in the sliding window process. ε_B is supposed unbiased Gaussian and its covariance matrix B is chosen as follow: $\begin{pmatrix} \infty & 0 \\ 0 & B_I \end{pmatrix}$. In others words, $\mathbf{w}(t_0)$ is not constrained to remain close to $\mathbf{w}_b$.

In Eq. (3), $\mathbb{H}$ stands for the observation operator: it projects the state vector in the vectorial space of the observations. In this particular case, $\mathbb{H}(\mathbf{X}) = I$. The equation Eq. (3) expresses that the synthetic images I should be close to the images acquired at times t_i. ε_R is also supposed unbiased Gaussian and described by its covariance matrix R.

Eqs. (1,2,3) are solved with a variational approach by minimizing the cost function J:

$$J(\mathbf{X}(t_0)) = \int_\Omega \varepsilon_B(\mathbf{x})^T B(\mathbf{x})^{-1} \varepsilon_B(\mathbf{x}) d\mathbf{x} +$$
$$\int_\Omega \int_{t_0}^{t_3} \varepsilon_R(\mathbf{x},t)^T R^{-1}(\mathbf{x},t) \varepsilon_R(\mathbf{x},t) d\mathbf{x} dt \quad (4)$$

with the constraint of Eq. (1). It has been shown (Le Dimet and Talagrand, 1986) that gradient of J is:

$$\nabla J = B^{-1}(\mathbf{X}(t_0) - \mathbf{X}_b) + \lambda(t_0) \quad (5)$$

where λ is the adjoint variable, defined by:

$$\lambda(\mathbf{x}, t_3) = 0 \quad (6)$$

$$-\frac{\partial \lambda}{\partial t}(\mathbf{x},t) + \left(\frac{\partial \mathbb{M}}{\partial \mathbf{X}}\right)^* \lambda(\mathbf{x},t) = \left(\frac{\partial \mathbb{H}}{\partial \mathbf{X}}\right)^* R^{-1}(\mathbf{x},t)$$
$$\times (\mathbb{H}(\mathbf{X})(\mathbf{x},t) - O(\mathbf{x},t)) \quad (7)$$

$\left(\frac{\partial \mathbb{M}}{\partial \mathbf{X}}\right)^*$ is the adjoint operator. It is formally defined as the dual operator of $\frac{\partial \mathbb{M}}{\partial \mathbf{X}}$ and the same applies for $\left(\frac{\partial \mathbb{H}}{\partial \mathbf{X}}\right)^*$. Reader should notice that the computation of $\lambda(\mathbf{x},t)$ is backward in time, from t_3 up to t_0. The approach is named 4D-Var (Courtier et al., 1994) in the data assimilation literature.

ME obtained with a variational data assimilation technique is summarized in Algorithm 1.

Algorithm 1: Motion Estimation (ME).

Require: : $\mathbf{X}_b, O(t_1), O(t_2), O(t_3), B, R, MaxIter$
1: Set the iteration index $k = 0$
2: Initial condition of state vector $\mathbf{X}^k(t_0) = \mathbf{X}_b$
3: **repeat**
4:     Forward integration: compute $\mathbf{X}^k(t)$ for all time with Eq. (1), and compute J^k
5:     Backward integration: compute $\lambda^k(t)$ for all time with Eqs. (6,7) and compute ∇J^k
6:     Update state vector $\mathbf{X}(t_0)$ with the L-BFGS solver:

$$\mathbf{X}(t_0)^{k+1} = LBFGS(\mathbf{X}(t_0)^k, J^k, \nabla J^k)$$

7:     k=k+1
8: **until** $|\nabla J^k| < \varepsilon$ or $k > MaxIter$
9: **return** $\mathbf{X}(t_0)^k$

The numerical implementation of the model $\mathbb{M}$ is obtained with finite difference techniques and a semi-Lagrangian scheme. The discrete adjoint of the discrete model $\mathbb{M}$ is obtained from an automatic differential software. The choice of the covariance matrices values B and R depends on the type of data and is discussed in Section 5.

3.2 Forecasting

The last available observation $O(t_3)$ is then extrapolated over time, thanks to the velocity map computed by the ME algorithm, $\mathbf{w}_{ME}$: Eq. (1) is integrated in time from its initial condition:

$$\mathbf{X}(t_3) = \begin{pmatrix} \mathbf{w}_{ME} \\ O(t_3) \end{pmatrix} \quad (8)$$

$$\frac{\partial \mathbf{X}}{\partial t}(\mathbf{x},t) + \mathbb{M}_f(\mathbf{X})(\mathbf{x},t) = 0 \quad \forall t > t_3 \quad (9)$$

If the time horizon is large, the hypothesis of stationary motion is no more valid and the heuristic of Lagrangian constancy of $\mathbf{w}$ is chosen. This is described by the non-linear advection equation $\frac{\partial \mathbf{w}}{\partial t} + \nabla \mathbf{w}.\mathbf{w} = 0$. The numerical model $\mathbb{M}$ is then slightly modified to obtain $\mathbb{M}_f = \begin{pmatrix} \nabla \mathbf{w}.\mathbf{w} & \nabla I.\mathbf{w} \end{pmatrix}^T$ with non-linear advection on $\mathbf{w}$, see (Lepoittevin and Herlin, 2015).

4 MULTISCALE RAIN NOWCASTING

4.1 Sequential Approach for ME

This section presents a first approach for the estimation of motion from multiscale image, with the objective of improving the performance of Rain Nowcast, thanks to the simultaneous use of local and regional data. In the following we both make use of *regional data*, denoted by a r exponent, and *local data*, denoted by a l exponent. Motion estimation includes two phases. In the first phase, the motion field $\mathbf{w}^r$ is estimated from the regional images. $\mathbf{w}^r$ is then oversampled to the local resolution, and used as background for the second phase: motion estimation on the local image. This second phase computes a refinement of the regional estimation from the local data with a finer spatial resolution. Algorithm 2 illustrates the principle of the method, where $\uparrow$ stands for the oversampling operator.

This approach is fully sequential as it requires the estimation of the regional motion field before computing the local one. As pointed out in the previous section, motion estimation includes a set of parameters depending on the type of input data. In this sequential approach, the two phases apply independently, consequently allowing to define independent parameters, suited for the data types.

Algorithm 2: Sequential Multiscale Motion Estimation.

1: Read the regional acquisitions $O^r(t_i)_{i=\{0,1,2,3\}}$
2: Set the values of regional covariance matrices B^r and R^r
3: Set the initial background

$$\mathbf{X}_b^r = \begin{pmatrix} \mathbf{w}^r(t_0) & O^r(t_0) \end{pmatrix}^T$$

4: Regional estimation

$$\mathbf{X}^r(0) = \text{ME}(\mathbf{X}_b^r, O^r(t_i)_{i=\{1,2,3\}}, B^r, R^r, MaxIter)$$

5: Oversample the regional estimation to local resolution (1 km to 200 m) $\mathbf{w}^l(t_0) = \uparrow \mathbf{w}^r(t_0)$
6: Read the local acquisitions $O^l(t_i)_{i=\{0,1,2,3\}}$
7: Set the values of local covariance matrices B^l, R^l
8: Set the initial background

$$\mathbf{X}_b^l = \begin{pmatrix} \mathbf{w}^l(t_0) & O^l(t_0) \end{pmatrix}^T$$

9: Local refinement

$$\mathbf{X}(0) = \text{ME}(\mathbf{X}_b^l, O^l(t_i)_{i=\{1,2,3\}}, B^l, R^l, MaxIter)$$

4.2 Parallel Approach for ME

Another way to tackle this problem is to simultaneously assimilate local and regional data: the image acquisitions of the two radars do not have the same spatial resolution but they are assimilated for producing a velocity map at the X-BAND resolution. The regional data of PANTHER are then first oversampled at the local resolution. A Gaussian blur, with a standard deviation of 5, is then applied on the result for avoiding the aperture problem (Beauchemin and Barron, 1995) occurs when pixels are duplicated with the same value. At that stage, local and regional data have the same resolution and can be simultaneously assimilated with the model.

The state vector is extended with a fourth component I^r: a synthetic image having the same resolution than the local data and close to values of the regional data. The synthetic local data is denoted I^l. The state vector is given by:

$$\mathbf{X}(\mathbf{x},t) = \begin{pmatrix} \mathbf{w}(\mathbf{x},t) \\ I^l(\mathbf{x},t) \\ I^r(\mathbf{x},t) \end{pmatrix} \quad (10)$$

With the same formalism and notations than Subsection 3.1, we extend the operators $\mathbb{M}$ and $\mathbb{H}$. The evolution of the state vector is given by:

$$\frac{\partial \mathbf{w}}{\partial t} + \nabla \mathbf{w}.\mathbf{w} = 0 \quad (11)$$

$$\frac{\partial I^l}{\partial t} + \nabla I^l.\mathbf{w} = 0 \quad (12)$$

$$\frac{\partial I^r}{\partial t} + \nabla I^r.\mathbf{w} = 0 \quad (13)$$

and $\mathbb{M}(\mathbf{X}) = \begin{pmatrix} \vec{0} & \nabla I^l.\mathbf{w} & \nabla I^r.\mathbf{w} \end{pmatrix}^T$. $\mathbb{H}(\mathbf{X})$ writes:

$$\mathbb{H}(\mathbf{X}) = \begin{pmatrix} I^l & I^r \end{pmatrix}^T \qquad (14)$$

Observations are given by a 2-component image including the local and regional data: $O(t) = \begin{pmatrix} O^l(t) & O^r(t) \end{pmatrix}^T$. The covariance matrix R is then defined by:

$$R = \begin{pmatrix} R^l & 0 \\ 0 & R^r \end{pmatrix} \qquad (15)$$

The background value $\mathbf{X}_b$ is extended to $\begin{pmatrix} \mathbf{w}_b & I^l_b & I^r_b \end{pmatrix}^T$ and initialized by: $\begin{pmatrix} \mathbf{w}_b & O^l(t_0) & O^r(t_0) \end{pmatrix}$. The covariance matrix B writes:

$$\begin{pmatrix} \infty & 0 & 0 \\ 0 & B_{I^r} & 0 \\ 0 & 0 & B_{I^l} \end{pmatrix}. \qquad (16)$$

The challenge of this approach is to accurately tune the covariance matrices between the local and the regional scales. This method has the advantage to be faster than the sequential one, especially if distributed on several cores.

4.3 Multiscale Forecasting

The process of forecasting in a multiscale context is similar to the one described in Subsection 3.2. Both local and regional data are extrapolated in time using the velocity map computed by one of the two multiscale methods. Computing the forecast both local and regional scale allows to evaluate the methods from different criteria, as discussed in the next section.

5 RESULTS

For evaluating the two multiscale methods, denoted SMRN for Sequential Multiscale Rain Nowcasting and PMRN for Parallel Multiscale Rain Nowcasting, we compare their forecast results with those of Rain Nowcasting (RN), described in Section 3. The following four metrics are taken from the state-of-the-art (Shi et al., 2017): probability of detection (POD), Figure Merit in Space (FMS), False Alarm Rate (FAR) and Mean Absolute Error (MAE).

Pixels from the forecasted and ground truth images are classified as rain (1) and no-rain (0). The number of true positive TP (prediction=1, ground truth=1), true negative TN (prediction=0, ground truth=0), false positive FP (prediction=1, ground truth=0) and false negative FN (prediction=0, ground truth=1) is then calculated. Three metrics derive from

theses values: POD $= \frac{TP}{TP+FN}$ that measures the overlapping between observed structures and correct forecasted structures, FMS $= \frac{TP}{FP+FN+TP}$ that measures the overlapping between observed structures and forecasted structures, and FAR $= \frac{FP}{FP+TN}$ that measures the overlapping between wrong forecasted structures and forecasted structures. The last metric, MAE, is defined as the average squared error between the predicted rain rate and the observed one (ground truth). If good quality results, POD and FMS should be high, FAR and MAE low.

As two scales of images are included in the process, there are two ways for evaluating the methods. The first one compares the output of SMRN or PRMN with the output of RN obtained on local data. This allows to quantify the benefit of regional data. The metrics are then computed on the forecasted local data and on the local domain (the circular domains of the three X-BAND radars as showed in Figure 1). This is discussed in Subsection 5.1. The second way compares the output of SMRN or PRMN with the output of RN computed on regional data. This allows to quantify enhancement of regional data by local data. In that case, the metrics are computed on the forecasted regional data but still on the local domain. This is discussed in Subsection 5.2.

Our data set is divided in three sequences with a total of 612 images for both scales. In this paper the statistics and figures only come from the second event (24 to 25th June, 2016). Nevertheless the results for the two other sequences remains similar. This sequence is chosen for two reasons: first, observed events are quite typical; second, several cells are visible with high velocities.

5.1 Evaluation on Local Spatial Domain

An important requirement of the method is the tuning of the parameters. In particular, matrices B^l_I, B^r_I, R^l and R^r should be correctly initialized according to the type of data. In this application, the tuning concerns the precision on the rain values. $R^l(\mathbf{x}, t_i)$ is consequently taking into account the rain/no-rain classification: high value if no-rain, low value otherwise. This means that only significant rainfall quantities will be assimilated. The same applies for R^r and regional data. B^l_I and B^r_I are set to a low value. This means that the I component of the state vector is forced to be close to local and regional backgrounds.

We display on Figures 2 and 3 the four chosen metrics for the results of SMRN and PMRN compared to RN, when computing a forecast at 15 minutes horizon from each image of the sequence (apart the first 6 ones that are used for initializing the sliding window:

graphics begin at 7). We also computed the forecasts at 1 hour and 15 minutes horizon (making the comparison with ground truth not possible on the last 10 ones: graphics end at 138).

The part on local data of Table 1 gives the statistics for the whole sequence and shows that the performances of SMRN and PMRN are better than those of RN. This is first due to the fact that the motion of the structures located on the boundary of the local domain (purple contours depicted in Figure 4) is better estimated if making use of the regional data. Moreover, the quantity of forecasted rain is more accurate if it is entering the local domain: it is estimated from the rain that is observed on regional data outside the local domain. Statistics given in Table 2 confirm this improvement. Another improvement is a better estimation of motion inside the local domain, leading to a better forecast: forecasted rain structures are more correlated to the ground truth.

Table 1: Comparison of average scores on local and regional data.

		POD	FMS	FAR	MAE
Local data	RN	0.421	0.270	0.522	0.885
	SMRN	0.445	0.290	0.513	0.880
	PMRN	0.438	0.290	0.511	0.877
Reg. data	RN	0.439	0.332	0.423	0.682
	SMRN	0.475	0.365	0.386	0.665
	PMRN	0.442	0.342	0.390	0.674

Table 2: Comparison of metrics scores with local data on 06/24/2016 at 07:45 and on 06/25/2016 at 17:35.

		POD	FMS	FAR	MAE
06/24 07:45	RN	0.608	0.420	0.417	1.740
	SMRN	0.648	0.420	0.448	1.573
	PMRN	0.654	0.440	0.415	1.707
06/25 17:35	RN	0.346	0.190	0.702	0.695
	SMRN	0.373	0.210	0.667	0.684
	PMRN	0.348	0.190	0.688	0.663

5.2 Evaluation on Regional Spatial Domain

The forecast performances are now analyzed in comparison with the regional data. The goal is to evaluate the benefit of adding local data for regional forecasting applications. Local and regional covariance matrices R and B are set to the same values than in the previous subsection.

It can be seen on Figures 5, 6 and in the regional part of Table 1 that SMRN and PMRN provide the best results. Improvements are located inside the local domain: the forecasted rain structures are better correlated to the ground truth as illustrated in Figure 7
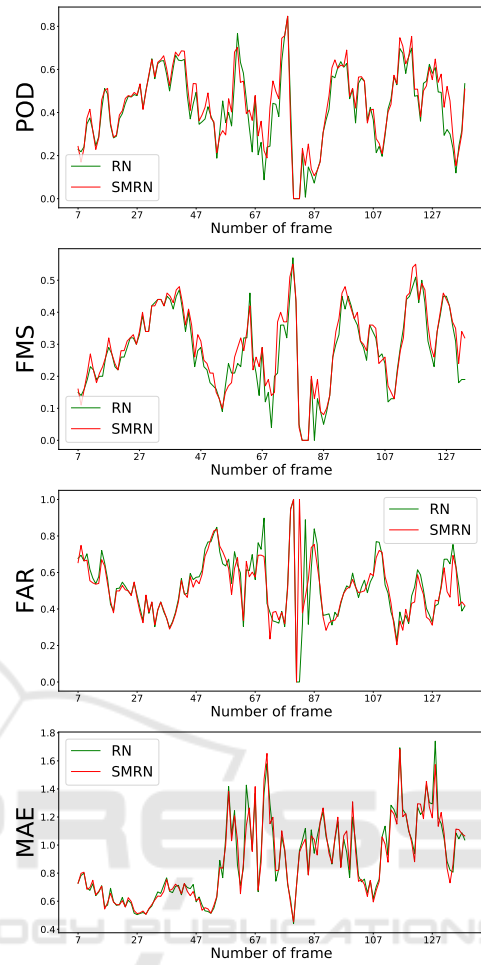

Figure 2: Results of SMRN at 15 minutes horizon on local data.

Table 3: Comparison of metrics scores with regional data on 06/24/2016 at 07:45 and on 06/25/2016 at 17:35.

		POD	FMS	FAR	MAE
06/24 07:45	RN	0.623	0.500	0.276	1.294
	SMRN	0.668	0.540	0.244	1.182
	PMRN	0.649	0.530	0.250	1.291
06/25 17:35	RN	0.271	0.200	0.544	0.604
	SMRN	0.356	0.270	0.457	0.554
	PMRN	0.315	0.240	0.479	0.617

and Table 3. This is due to the better accuracy of the local data (better spatial resolution) compared to the regional ones. Outside the local domain, the regional data being the only available, the use of local data by our approach does not impact the results of SMRN and PMRN.
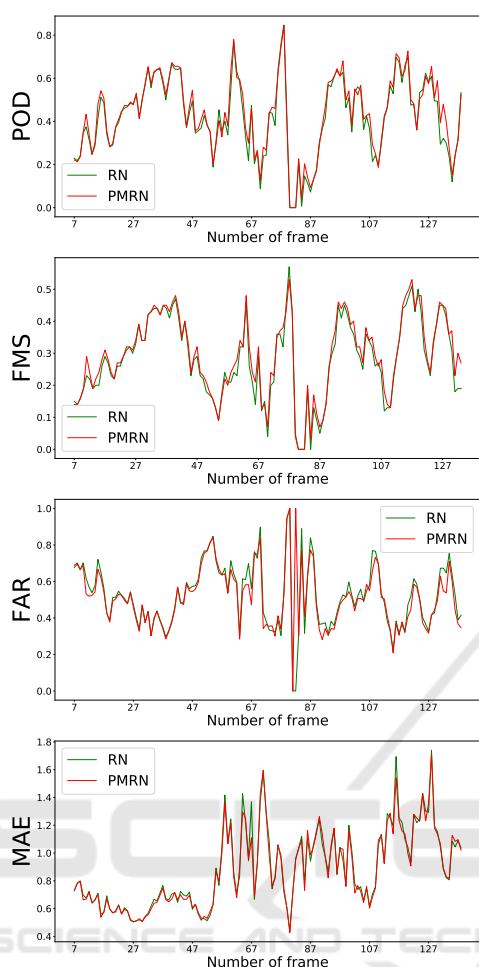
Figure 3: Results of PMRN at 15 minutes horizon on local data.
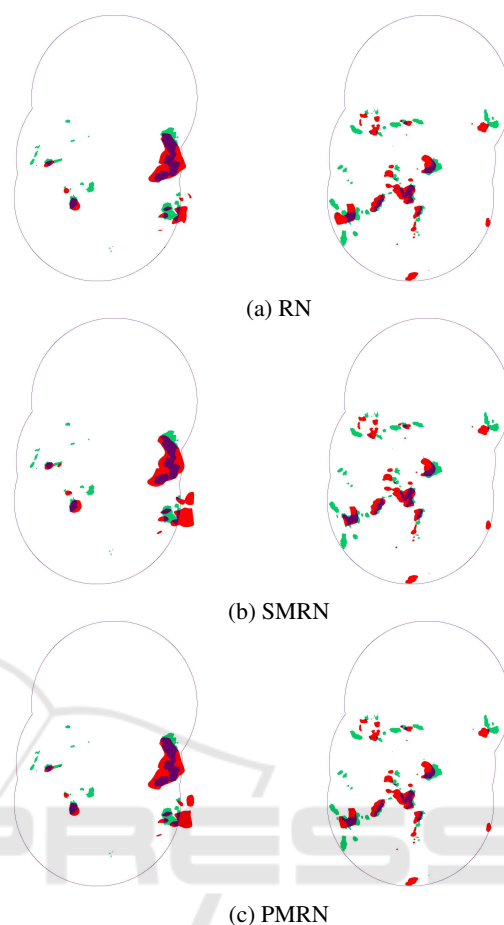

(a) RN

(b) SMRN

(c) PMRN

Figure 4: 15 minutes horizon forecast for local data computed by RN, SMRN and PMRN. Left column: on 06/24/2016 at 07:45, right column: on 06/25/2016 at 17:35. Ground truth is in green, forecast in red and their intersection in purple.

6 CONCLUSION AND FUTURE WORKS

This paper described two rain nowcast multiscale method applied on two types of radar data: regional data with a rough spatial resolution and local data with a fine spatial resolution, on a smaller spatial domain. We showed the improvement of these multiscale methods compared to an operational one applied on only local high resolution data. We illustrated the performance of these approaches when forecasting at a short temporal horizon of 15 minutes. Up to 45 minutes, conclusions remain quite similar but the quality of forecast decreases.

Over 45 minutes, our methods provide low quality results, due to the numerical scheme chosen for approximating advection of motion and reflectivity data during the forecast process. This semi-Lagrangian scheme, being implicit, has the major advantage not be constrained to CFL conditions. This allow using a high value time step and consequently reducing the global computational requirements. However, this scheme has the drawback to smooth (and consequently to suppress) the rain structures if applied for a long temporal horizon. In a future work, alternative numerical schemes will be investigated.

Another issue concerns the lower performance of PMRN compared to SMRN one. However, PMRN remains promising because it is faster than SMRN. Additional research work should be considered for the definition of the covariance matrix R. Radars from the PANTHERE regional network do not see the same structures than the local X-BAND radars: the altitude of the signal acquisition is depending on the distance between the radar and the rainfall event. This property may introduce contradictions during the optimization phase of data assimilation as a unique motion field is
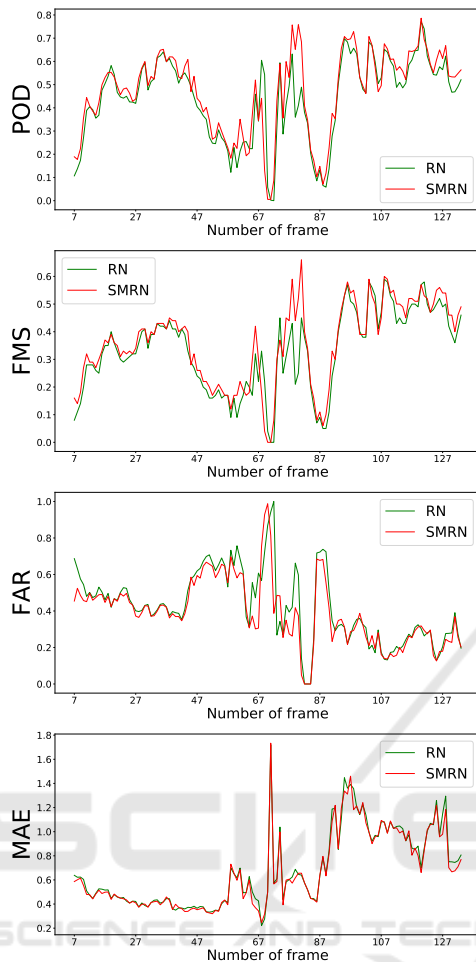
Figure 5: Results of SMRN forecast at 15 minutes horizon on regional data.

Figure 6: Results of PMRN forecast at 15 minutes horizon on regional data.

not able to correspond to different structures in the local and regional data. A weighting coefficient must be applied between the local and regional data that should be expressed by the matrices R^l and R^r.

REFERENCES

Beauchemin, S. and Barron, J. (1995). The computation of optical flow. *ACM Computing Surveys*, 27(3).

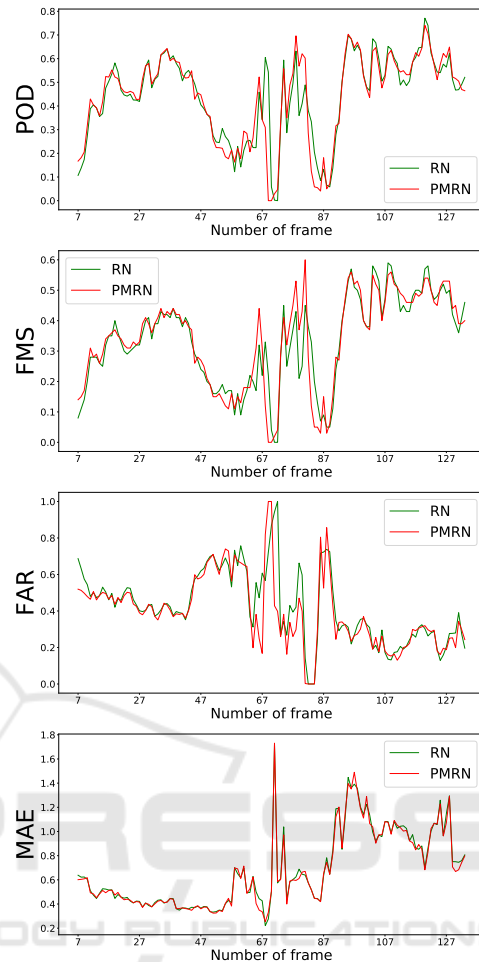Berenguer, M., Sempere-Torres, D., and Pegram, G. G. (2011). Sbmcast – an ensemble nowcasting technique to assess the uncertainty in rainfall forecasts by lagrangian extrapolation. *Journal of Hydrology*, 404(3):226 – 240.

Béréziat, D., Herlin, I., and Younes, L. (2000). A Generalized Optical Flow Constraint and its Physical Interpretation. In *Proceedings of the conference on Computer Vision and Pattern Recognition*, volume 2, pages 487–492, Hilton Head, SC, United States. IEEE.

Béréziat, Herlin, I. (2018). Motion and acceleration from image assimilation with evolution models. *Digital Signal Processing*, 83:45–58.

Bowler, N., Pierce, C., and Seed, A. (2004). Development of a rainfall nowcasting algorithm based on optical flow techniques. *Journal of Hydrology*, 288:74–91.

Corpetti, T., Héas, P., Memin, E., and Papadakis, N. (2009). Pressure image assimilation for atmospheric motion estimation. *Tellus A*, 61(1):160–178.

Courtier, P., Thépaut, J.-N., and Hollingsworth, A. (1994). A strategy for operational implementation of 4D-Var, using and incremental approach. *Quaterly Journal of the Royal Meteorological Society*, 120(1367–1387).

Dixon, M. and Wiener, G. (1993). Titan: Thunderstorm identification, tracking, analysis, and nowcasting—a
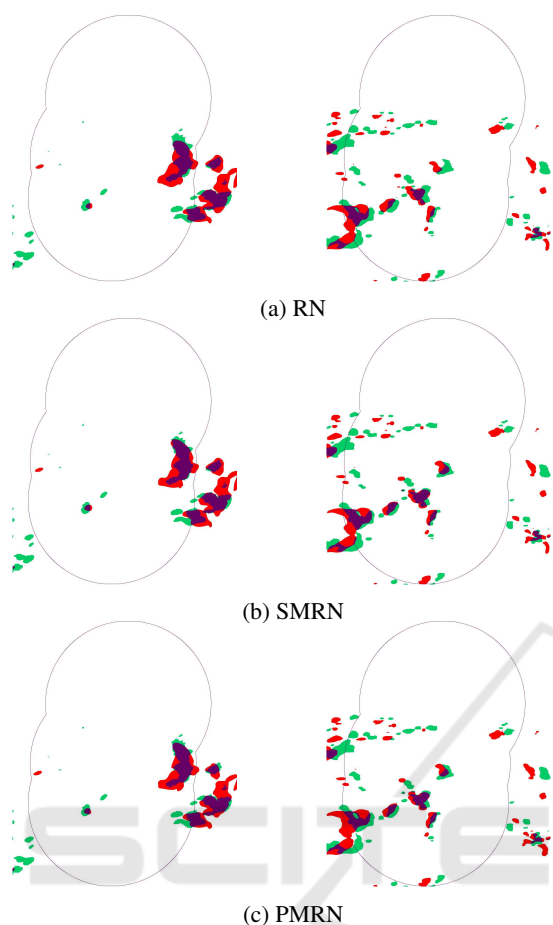
(a) RN

(b) SMRN

(c) PMRN

Figure 7: 15 minutes horizon forecast for regional data computed by RN, SMRN and PMRN. Left column: on 06/25/2016 at 17:35, right column: on 06/24/2016 at 07:45.

radar-based methodology. *Journal of Atmospheric and Oceanic Technology*, 10:785.

Germann, U. and Zawadzki, I. (2002). Scale-dependence of the predictability of precipitation from continental radar images. part i: Description of the methodology. *Monthly Weather Review - MON WEATHER REV*, 130.

Héas, P., Memin, E., Papadakis, N., and Szantai, A. (2007). Layered estimation of atmospheric mesoscale dynamics from satellite imagery. *IEEE Transactions on Geoscience and Remote Sensing*, 45(2)(12):4087–4104.

Horn, B. and Schunk, B. (1981). Determining optical flow. *Artificial Intelligence*, 17:185–203.

Huot, E., Herlin, I., and Papari, G. (2013). Optimal Orthogonal Basis and Image Assimilation: Motion Modeling. In *ICCV - International Conference on Computer Vision*, Sydney, Australia. IEEE.

Joe, P., Dance, S., Lakshmanan, V., Heizenreder, D., James, P., Lang, P., Hengstebeck, T., Feng, Y., Li, P., Yeung, H.-Y., Suzuki, O., Doi, K., and Dai, J. (2012). Automated processing of doppler radar data for severe weather warnings. In Bech, J. and Chau, J. L., editors, *Doppler Radar Observations*, chapter 2. IntechOpen, Rijeka.

Johnson, J. T., MacKeen, P. L., Witt, A., Mitchell, E. D. W., Stumpf, G. J., Eilts, M. D., and Thomas, K. W. (1998). The storm cell identification and tracking algorithm: An enhanced wsr-88d algorithm. *Weather and Forecasting*, 13(2):263–276.

Korotaev, G. K., Huot, E., Le Dimet, F.-X., Herlin, I., Stanichny, S., Solovyev, D., and WU, L. (2008). Retrieving ocean surface current by 4-D variational assimilation of sea surface temperature images. *Remote Sensing of Environment*, 112(4):1464–1475. Remote Sensing Data Assimilation Special Issue.

Le Dimet, F.-X., Antoniadis, A., Ma, J., Herlin, I., Huot, E., and Berroir, J.-P. (2006). Assimilation of images in geophysical models. In *Conference on International Science and Technology for Space*, Kanazawa, Japan.

Le Dimet, F.-X. and Talagrand, O. (1986). Variational algorithms for analysis and assimilation of meteorological observations: Theoretical aspects. *Tellus*, 38A:97–110.

Lepoittevin, Y., Béréziat, D., Herlin, I., and Mercier, N. (2013). Continuous tracking of structures from an image sequence. In *VISAPP - 8th International Conference on Computer Vision Theory and Applications*, pages 386–389, Barcelone, Spain. Springer Verlag.

Lepoittevin, Y. and Herlin, I. (2015). Assimilation of radar reflectivity for rainfall nowcasting. In *IGARSS - IEEE International Geoscience and Remote Sensing Symposium*, pages 933–936, Milan, Italy.

Marshall, S. and Palmer, K. (1948). The distribution of raindrops with size. .*J. Metrol.*, 5.

Shi, X., Gao, Z., Lausen, L., Wang, H., and Yeung, D.-Y. (2017). Deep learning for precipitation nowcasting: A benchmark and a new model. In *31st Conference on Neural Information Processing Systems*.

Stigter, C. J., Sivakumar, M. V. K., and Rijks, D. A. (2000). Agrometeorology in the 21st century: workshop summary and recommendations on needs and perspectives. *Agricultural and Forest Meteorology*, 103(1/2):209–227.

Titaud, O., Vidard, A., Souopgui, I., and Le Dimet, F.-X. (2010). Assimilation of Image Sequences in Numerical Models. *Tellus A*, 62(1):30–47.